metals

MDPI

Article

Effect of Thermal Cycling on Grain Evolution and Micro-Segregation in Selective Laser Melting of FGH96 Superalloy

Lin Li [1,2,3], Furong Liu [1,2,3,*], Shijin Nie [1,2,3], Qin Wang [1,2,3], Rongxia Zhao [1,2,3], Yongzhi Zhang [1,2,3], Haoyuan Feng [1,2,3] and Xin Lin [4]

[1] Key Laboratory of Trans-Scale Laser Manufacturing, Beijing University of Technology, Ministry of Education, Beijing 100124, China
[2] Beijing Engineering Research Center of Laser Technology, Beijing University of Technology, Beijing 100124, China
[3] Institute of Laser Engineering, Faculty of Materials and Manufacturing, Beijing University of Technology, Beijing 100124, China
[4] State Key Laboratory of Solidification Processing, Northwestern Polytechnical University, Xi'an 710072, China
* Correspondence: liufr@bjut.edu.cn

Abstract: Extremely rapid heating and cooling rates during the additive manufacturing (AM) process generate complicated thermal cycles, which affect the microstructure evolution and ultimate mechanical properties of the alloy. In this paper, FGH96 blocks with a height of 6 mm were prepared by selective laser melting (SLM) and the microstructure was characterized by scanning electron microscopy (SEM) and transmission electron microscopy (TEM). Comparing specimens of varying heights, it was found that subsequent thermal cycles (STC) coarsened some solidified grains and accelerated the grain growth along the build direction, together with an increase in texture intensity and high-angle grain boundaries (HAGBs). After coarsening the grains in the middle portion of the built block, finer grains were observed near the top area due to a faster cooling rate. There were numerous dislocations in the grain because of the occurrence of unequal internal tension. In the middle of the sample with stable thermal cycles, the dislocations were both perpendicular to the grain growth direction and 45° off it. In spite of the texture characteristics, the segregation of elements was also found to be influenced by thermal cycling. Inherent reheating leads to the increase in the Laves phase and the decrease in the γ′ phase as subsequent deposition. This was also one of the reasons why the microhardness of the sample decreased as the building height and the other reason being the decrease in the solution treatment of the later sediments.

Keywords: selective laser melting; thermal cycles; microstructure evolution; micro-segregation

check for updates

Citation: Li, L.; Liu, F.; Nie, S.; Wang, Q.; Zhao, R.; Zhang, Y.; Feng, H.; Lin, X. Effect of Thermal Cycling on Grain Evolution and Micro-Segregation in Selective Laser Melting of FGH96 Superalloy. *Metals* **2023**, *13*, 121. https://doi.org/10.3390/met13010121

Academic Editor: Menachem Bamberger

Received: 7 December 2022
Revised: 31 December 2022
Accepted: 3 January 2023
Published: 7 January 2023

Copyright: © 2023 by the authors. Licensee MDPI, Basel, Switzerland. This article is an open access article distributed under the terms and conditions of the Creative Commons Attribution (CC BY) license (https://creativecommons.org/licenses/by/4.0/).

1. Introduction

Additive manufacturing (AM) has developed rapidly in recent years, due to its characteristics of "line-by-line and layer-by-layer" freely manufacturing parts of any shape [1]. Due to the small laser spot size, selective laser melting (SLM), a crucial technology in metal additive manufacturing, can accomplish high precision and arbitrary formation of complex parts [2,3]. The SLM process is often accompanied by fast heating and cooling under rapid laser scanning, resulting in an extremely complex thermal process [4–6]. Heat is mainly transferred through heat conduction and convection [7] in all directions. Under such conditions, the grain structures of the preceding layer may recrystallize under the heat effect of the succeeding layers. When there is a similar temperature differential between adjacent layers, even after grain epitaxial growth has occurred, the dendrite orientation of the following layers is also affected to some extent by the orientation of the previous layer's dendrites. Therefore, thermal cycling controls grain epitaxial growth and metallurgical bonding properties between adjacent tracks and layers [8].

Considerable previous work [9–14] has been performed to study the effect of thermal cycles in SLM. Huang et al. [9] demonstrated that due to the influence of the subsequent thermal cycle, the molten pools' temperature gradient and the cooling rate of the molten pool decreased with the increase of the layer number. Further, Yang et al. [10] prepared thin-wall parts of IN718 alloy and showed that the microstructure evolution of the central region of the thin wall is closely related to the vertical thermal cycle.

The effect of thermal cycling on the alloy's microstructure will alter its the mechanical properties. Mohamad Mahmoudi [11] suggested that the austenite content of the alloy was increased by thermal cycling, which leads to a decrease of hardness. Gunther Mohr [12] et al. found that when heat downward conduction was impeded, surface temperature, molten pool size and porosity at the top of the fabricated part all increased. However, Wang et al. [13,14] investigated the influence of thermal cycling on the grain texture of IN718 alloy and found that the mechanical properties did not change significantly with the building height. Consequently, there are some disagreements regarding the relationship between thermal cycling and alloy properties along the building height, which is also the subject of our research.

The most widespread application of SLM is in the aerospace industry, where the manufacturing of nickel-based superalloys accounts for a large part of its use. Superalloy refers to the type of alloy that can be utilized reliably in high temperature environments above 600 °C, and has excellent mechanical properties such as oxidation resistance, fatigue resistance, creep resistance and wear resistance [15,16]. Nickel-based alloy is the most complex in composition, but also the most widely studied and applied in the aerospace field. Its high strength is due to its high content of refractory elements, such as Co, Cr, Mo, W, etc. In addition, some alloys also have Ti-Al elements, which can produce γ′ hardening phase to improve the creep characteristics [16]. It is typically regarded as a kind of poor welding alloy due to its high content of Ti and Al elements content, which causes precipitation of high melting-point phases in the interdendritic region and some low melting-point strengthening phases in the dendritic trunk region [17], resulting in the initiation of cracks at grain boundaries when subjected to tensile stress [18,19]. Therefore, during the process of rapid laser processing, not only the grain evolution is complicated, but also the segregation of refractory elements, which determines that it is necessary to have a more in-depth understanding of the evolution law of the Al-Ni based superalloy microstructure under the thermal cycle.

FGH96, a typical Ni-base superalloy with high Ti/Al content, can operate in an environment of 650–750 °C for a long time as a hot-end component in the aero-engine for its high crack resistance, damage resistance and creep strength [20,21]. Up to date, most FGH96 parts have been manufactured by powder metallurgy (PM) [22] with few reported by additive manufacturing. Hao et al. [23–25] demonstrated that FGH96 can be fabricated by SLM and the effect of solution treatment on microstructure evolution was then studied.

In this paper, typical Nickel based superalloy FGH96 samples were prepared by SLM. The characteristic evolution of texture, dislocation and microsegregation under thermal cycling was analyzed. The results shed light on the relationship between the alloy's microstructure and the mechanical properties.

2. Experiment

The FGH96 powder used in the experiment was made by gas atomization. Table 1 shows its chemical composition. The powder is typically spherical with a smooth and neat surface, with only a small amount of satellite powders attached, as seen in Figure 1a. According to Figure 1b, the powder's size distribution ranges from 15 to 53 μm.

Table 1. Chemical composition of FGH96 powder (wt.%).

Element	Cr	Co	W	Mo	Ti	Al	Nb	C	Zr	Ni
wt.%	15.5–16.5	12.5–13.5	3.8–4.2	3.8–4.2	3.55–3.9	1.95–2.3	0.60–0.80	0.045–0.060	0.03–0.06	bal.

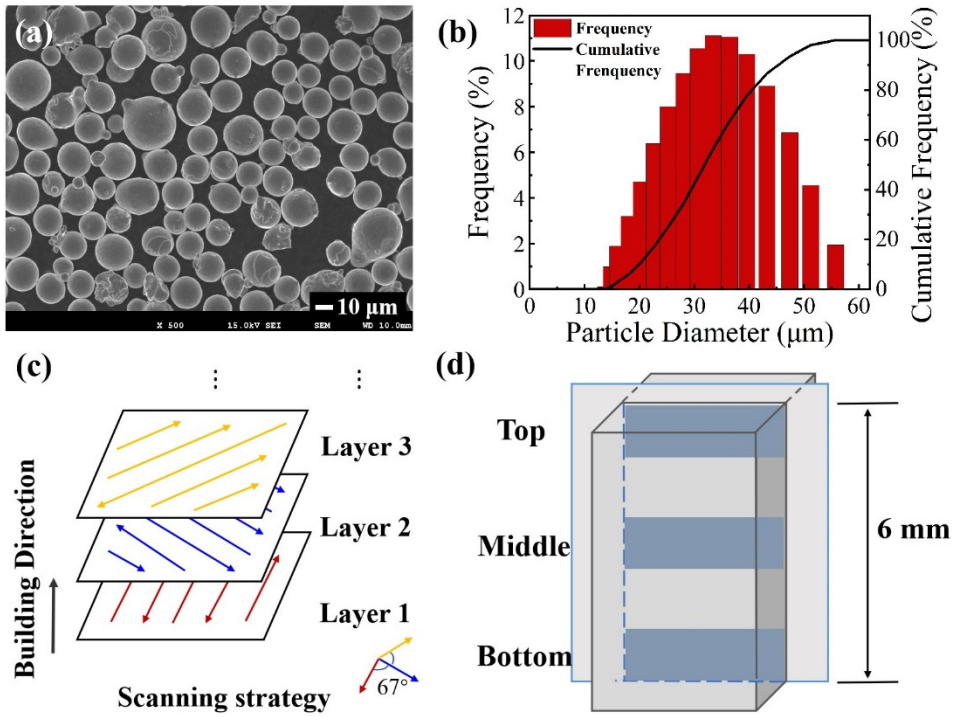


Figure 1. (**a**) Morphology of the FGH96 powder; (**b**) particle-size distribution; (**c**) scanning scheme for the layer-by-layer SLM process; (**d**) specimens chosen from different positions of the SLMed sample.

The AM blocks used in this study were manufactured by an EP-M260 (Beijing e-Plus 3D Tech. Co., LTD, Beijing, China) molding system, with a continuous wave fiber laser. The system was equipped with a molding chamber size of 266 mm × 266 mm × 390 mm. Ar was used as a protective gas, and the oxygen content in the chamber was less than 100 ppm. The scanning strategy and shape design are shown in Figure 1c. According to [26], the rotation angle between two adjacent deposition layers of 67° was chosen to obtain a better microstructure and properties. The sample size was 3 mm × 6 mm × 6 mm, and the microstructure evolution of the alloy was observed at the bottom, middle and top. The process parameters used in SLM are shown in Table 2.

Table 2. Parameters used in the experiment.

Analysis	Value
Laser power P/W	270
Scanning speed v/(mm/s)	1200
Layer depth d/μm	40
Interlayer rotation	67°
Hatch spacing h/μm	80

The samples were polished and then corroded with 5 g $CuSO_4$ + 25 mL HCl + 25 mL C_2H_5OH mixed solution to observe the detailed microstructure and texture. A scanning electron microscope (SEM, KSM-7610FPlus, JEOL, Tokyo, Japan) was used to observe the microstructure, crack morphology and distribution of precipitates. The texture and grain orientation morphology were detected by electron backscatter diffraction (EBSD, JSM-7001F, JEOL, Tokyo, Japan). The microscopic characteristics of the samples were observed by transmission electron microscope (TEM, JEM-2010, JEOL, Tokyo, Japan). A Vickers hardness tester (Wilson HV1102, Wilson, Norwood, MA, USA) was employed to measure the hardness of various specimens. The acting load was 500 g and the duration was 20 s. After that, Image-Pro Plus software [23] (Version 6.0, Media Cybernetics, Inc., Rockville,

MD, USA) was used to calculate the area fraction of Laves phases in SEM images and the average values from five repeated measurements were obtained.

3. Results and Discussion

3.1. Typical Microstructure Features of the FGH96 Building Block

Figure 2 shows the vertical section microstructure of the FGH96 sample under SEM observations, in which BD, SD and TD represent building direction, scanning direction and track moving direction, respectively. As depicted in Figure 2a, some grains as large as a few hundred microns are found to grow roughly in the direction of BD. During the solidification of molten pools, a large cooling gradient may be responsible for the occurrence of epitaxial growth in an upward direction. Figure 2b presents the morphology of each molten pool. As demonstrated in Figure 1c, the distribution of molten pools is intertwined due to the scanning scheme. The variance in the size of each molten pool is caused by the powder bed's spreading mechanism. Despite the randomness, it is evident that epitaxial growth happens through a significant number of layers. Figure 2c illustrates the precise microstructure distribution in a typical molten pool, with an even semi-elliptical form that is not symmetrical along the central line (the red dotted line plotted in Figure 2c). In addition, a residual thermal accumulation from the preceding deposition track causes the central line of the molten pool to tilt in the opposite direction of TD to the left. Simultaneously, the increased cooling rate and temperature gradient along the central line result in the rapid formation of columnar grains upwards towards the center of the molten pool [27], as shown by the blue lines in Figure 2c, caused by the Gaussian energy distribution of the laser beam. For the remelting sections of adjacent tracks in the yellow dotted lines, as shown in Figure 2d, overlapped heat input results in a reduced temperature gradient and cooling rate, leading to the construction of a structure that is both cellular and dendritic. A relatively moderate cooling gradient in these locations causes previously formed dendrites to remelt and eventually solidify into separate cellular structures, as shown in Figure 2d. However, the arrangement of the cellular crystals retains the shape of the dendrite, with the direction of growth rotated (~30°) toward the next track. Both the area of the cellular crystals and the arrangement angle are affected by the formation of columnar crystals near the center line, and the resulting temperature field.

The dark region in the SEM image with high magnification is the γ matrix [15], while the bright white lamellar areas on the dendrite trunks are the Laves phases at the end of solidification (Figure 2e) [10]. Besides, Figure 2f shows the discrete fine white granular precipitates distributed in the interdendritic regions, which are identified as MC carbide by EDS analysis in Figure 2g, presenting the segregation of C, Nb, Mo and Ti elements. It is difficult to distinguish carbides from γ′ phase because they have similar appearance, so we confirm the existence of γ′ by selective area electron diffraction (SAED) in TEM [28] as shown in Figure 3.

The EBSD measurements were used to characterize the texture of different specimens in the XOZ plane. Figure 4 shows the typical texture of FGH96. As can be seen from the inverse pole figure (IPF) in Figure 4a, grains in the XOZ plane present a strong <001> orientation [29]. Some of the elongated grains grew more than approximately 300 μm in length directionally, indicating that these grains maintain a certain growth orientation within seven layers (estimated from the 40 μm powder layer thickness). This is due to the extremely high temperature gradient and cooling rate during the melting and solidification process of the new layer, which makes the alloy unable to nucleate. Instead, the alloy grows epitaxial based on the dendrites of the front grains. However, these elongated grains show strong orientation of <001> and <101>. Figure 4b shows the grain boundary distribution, where the colors red, green, and blue represent three ranges of misorientation angles (the angles between the direction of the grain boundaries and <001> direction), namely low (2–5°), medium (5–15°) and high (15–180°) misorientation angles. Multiple low-angle grain boundaries are present at the high-angle grain boundary, indicating a significant number of sub-grains. The pole figures of <001>, <111> and <101> directions are shown in

Figure 4c. It can be seen from the projection position that the orientation distribution of the crystal has a certain symmetry, especially in the direction <001>, and its maximum texture strength is 12.723. Figure 4d,e depict the statistics of the grain size distribution and grain boundary misorientation angle, respectively. Most of the grain sizes are 30–140 μm with a few exceeding 200 μm. Nearly 36% of the grain boundary misorientation angles are within 5°, suggesting that the texture has an excellent <001> orientation.

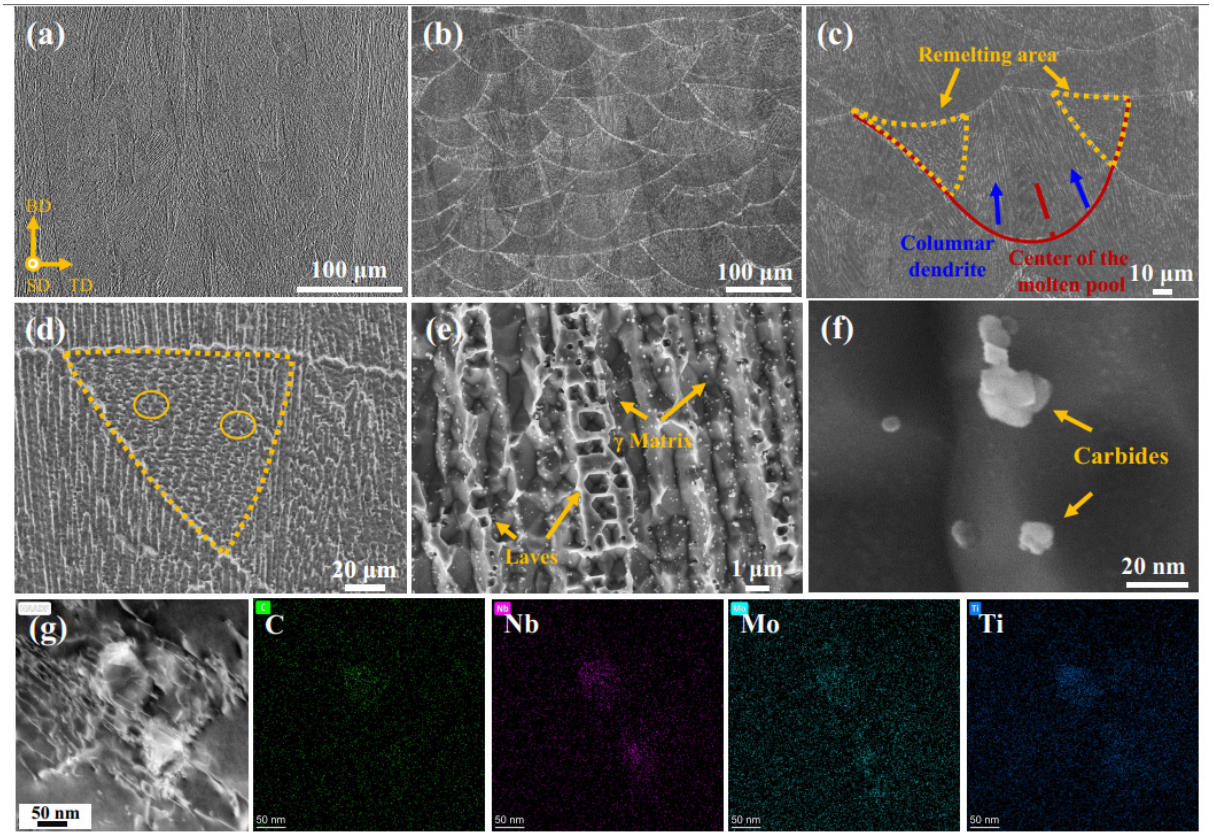


Figure 2. Microstructure analyses: (**a**) BSE and (**b**–**f**) SEM micrographs. (**g**) The EDS analysis for carbides.

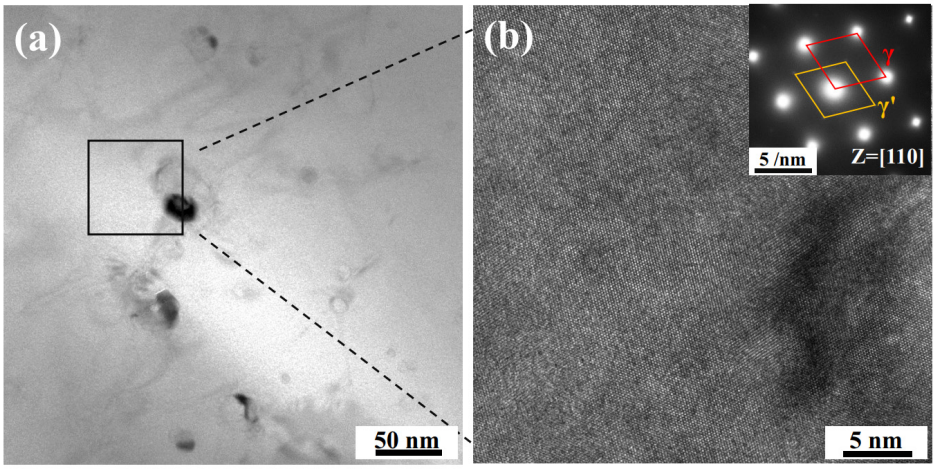


Figure 3. (**a**) Bright-field STEM image of FGH96 sample matrix and precipitations. (**b**) The corresponding SAED pattern of the region.

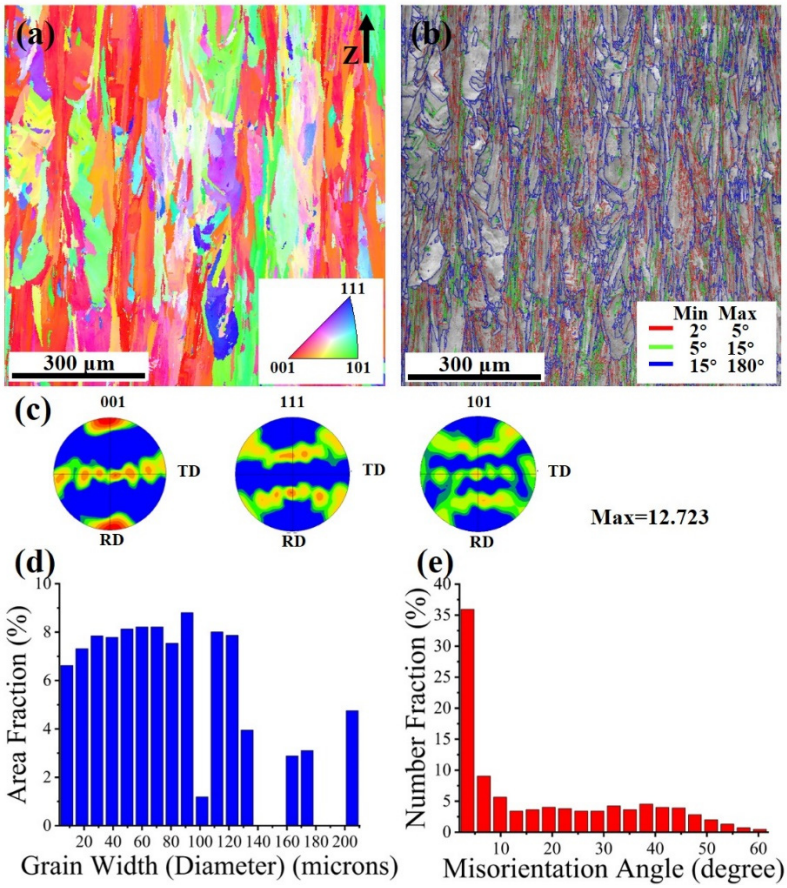


Figure 4. EBSD images of the FGH96 sample: (**a**) inverse pole figure; (**b**) grain boundary map; (**c**) pole figure; (**d**) grain size distribution; (**e**) misorientation angle statistics.

3.2. Microstructure Variation along the Building Direction

Figure 5 shows the EBSD images with different heights of bottom to top. It is found that the fractions of large-size grains (meaning more than 100 μm in diameter) are 40.4%, 52% and 30%, respectively, showing a trend of first-increase-and-then-decrease with the building height.

The crystal growth, including size and orientation, is determined by a combination of the temperature gradient, cooling rate and preferred crystal orientation [30]. The grain size is inversely proportional to the cooling rate. Through the heat conduction effect, more residual heat travels to the substrate and surrounding thin powder layers during the initial stage of printing (bottom). At this stage, it is easy to nucleate the grains. Thus, the growth is largely dependent on the substrate, with a smaller size and disorderly orientation (as shown in Figure 5a). When the accumulation reaches a certain height (middle), subsequent thermal cycling (STC) reduces the cooling rate to decrease and hence increases grain size. The substrate is no longer a factor in dendrite development. When the temperature gradient is similar to that of the layer immediately next, the solidification front will epitaxially follow the existing dendrite. The majority of sedimentary layers' greatest temperature gradient is vertical downhill, which causes the crystal to grow along the building direction and intensifies its <001> orientation texture. A higher cooling rate at top leads to some fine grains of the block because of the thermal convection near the top surface and the reduction in STC [31,32].

This trend of cooling rate can also be proved by the empirical formula of primary dendrite arm spacing (PDAS) and cooling rate, as shown in Formula (1) [33]. The average

PDAS of columnar grains measured by SEM at the three specimens and the cooling rates calculated are shown in Table 3.

$$\alpha = 104.47 \times R^{-0.31} \quad (1)$$

where α and R represent PDAS and cooling rate, respectively.

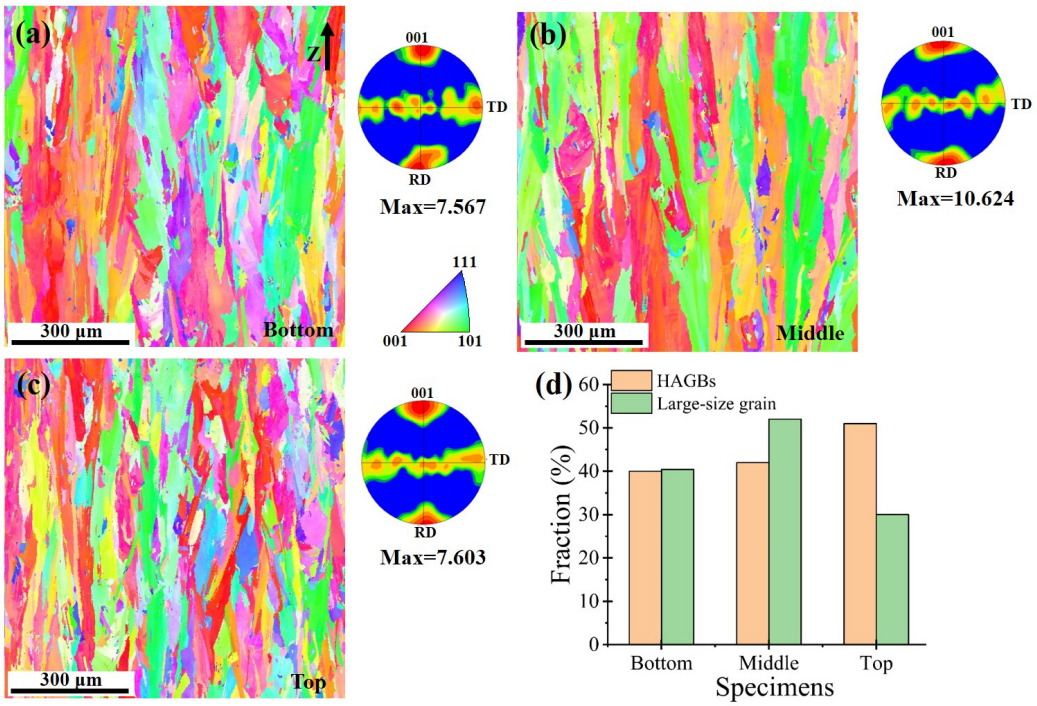


Figure 5. Comparison of the EBSD images for the three specimens with different heights: (**a**–**c**) the pole figure and inverse pole figure of bottom, middle and top, respectively; (**d**) statistics on the fraction of high-angle grain boundaries (HAGBs) and large-size grains (over 100 μm). Additional Supplementary data are shown in Figures S1–S3.

Table 3. Cooling rate predicted from experimental states.

Specimens	α_{ave} (μm)	R (°C/s)
Bottom	0.733	8.08×10^6
Middle	1.218	1.57×10^6
Top	0.915	4.34×10^6

However, the proportion of high angle grain boundaries (HAGBs) increases with the building height, as shown in Figure 5d. The misorientation angle can be utilized to characterize the strain distribution at the grain boundary of a deformed crystal material. This pattern can be described as a result of the accumulation of heat induced by layer-by-layer sedimentary accumulation, which increases the internal residual stress and grain boundary energy [34,35], leading to the increase in grain boundary mobility.

In fact, according to the previous report [15], the scanning strategy of interlayer rotation of 67° results in a grain texture intensity 3/10 of that of 90°. However, the experimental results show that compared with the 90° rotation, the irregular thermal cycle of 67° leads to the preferred growth of dendrites with different orientations, which refines grains and inhibits the vertical epitaxial growth and produces irregular columnar or equiaxial crystal structures. It also explains why the columnar dendrites can only extend through four ~ five layers of the molten pool. In addition, the disorderly grain boundaries inhibit the propagation of cracks.

Figure 6 shows the typical distribution characteristics of dislocations of SLMed FGH96 samples under TEM. As shown in Figure 6a, many dislocations are distributed in the matrix, and some are densely wound to form a "dislocation wall" whose arrangement direction is roughly parallel to that of sub-grain boundaries. Due to the uneven distribution of internal stress brought by the high thermal expansion and cooling shrinkage in the SLM process, atomic staggering develops during crystal formation [36]. A locally magnified dark-field TEM image can be seen in Figure 7b. Grain boundaries become tortuous due to the presence of precipitated phases, and solute segregation rises the structural stress of the matrix, resulting in dislocation winding [37], which plays the role of "pinning" strengthening on LAGBs and prevents grain boundaries from slippage.

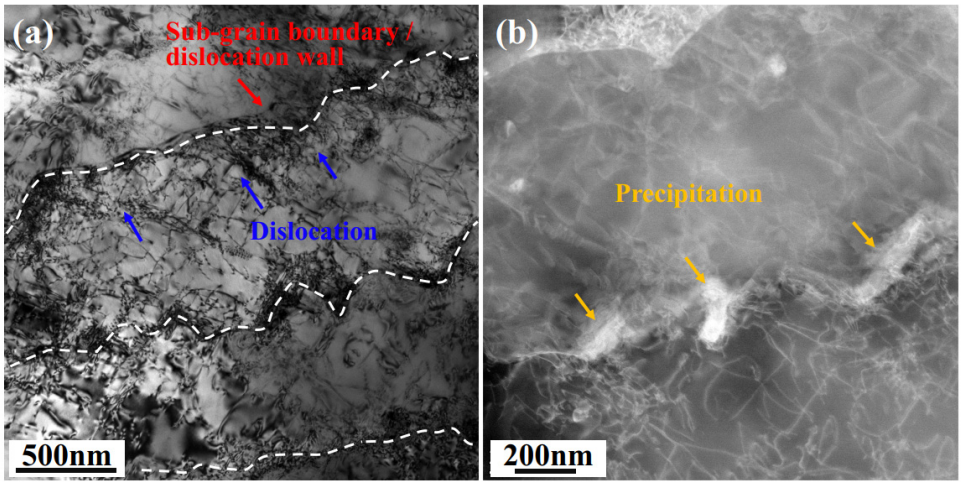


Figure 6. (**a**) TEM images containing grain boundaries and dislocations. (**b**) Dark-field image of the corresponding zone.

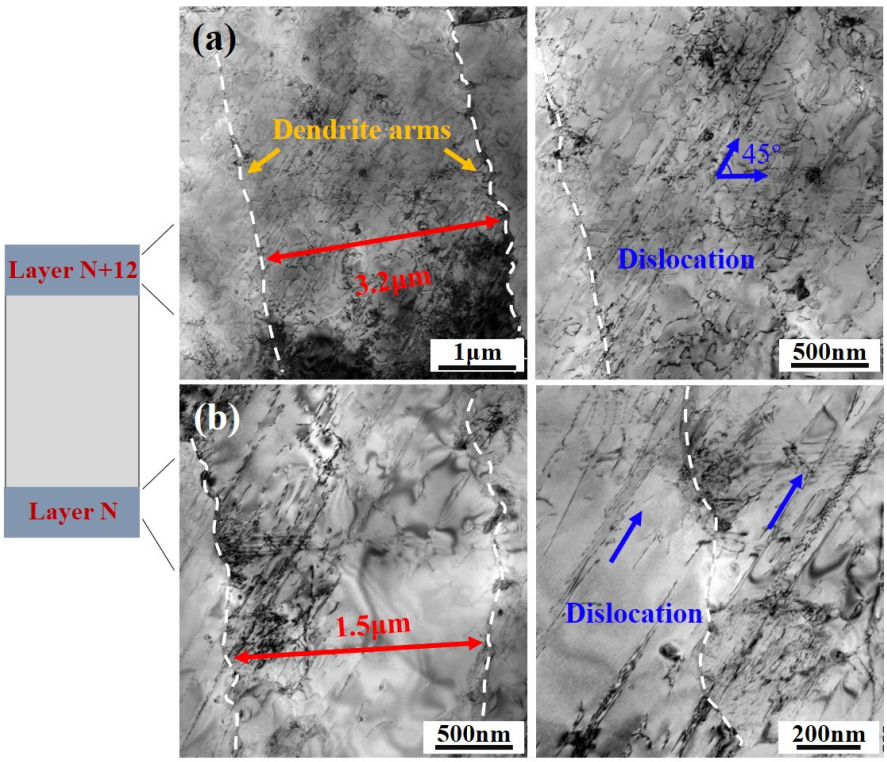


Figure 7. Dislocation distribution of (**a**) Layer N and (**b**) Layer N + 12.

The middle of the sample with a stable thermal cycle (Z ≈ 3 mm) was extracted, and the dislocation characteristics at a certain Layer N and the subsequent Layer N + 12 were observed, as shown in Figure 7. Here, the PDAs become bigger and bigger as the number of layers rises. Additionally, it is evident that dislocation occurs at Layer N at an angle of 45° to the direction of grain boundary as a result of the ongoing accumulation of energy and internal stress (Figure 7b). Furthermore, with the construction to Layer N + 12, another dislocation perpendicular to the dendrite arm was generated (Figure 7a). It is remarkable that the latter is restricted to a single large dendrite that begins and ends at the grain boundaries on both sides, whereas the former spans multiple grains.

3.3. Effect of Thermal Cycling on Segregation of Elements

Generally, the melting and solidification rate at the beginning stage is fast. Refractory elements (such as Nb, Ti and Mo) have no time to diffuse from the solid phase to the liquid phase [38], so that more refractory elements remain in the matrix and it is difficult to form the Laves phase [39]. As heat accumulates, the solidification rate lowers and there is sufficient time for element segregation, culminating in the L → γ + Laves transition between dendrites at the conclusion of solidification [10]. Figure 8a,b respectively exhibit the morphology of the two dislocation networks located at bottom and middle under HAADF, as well as the EDS analysis of the relevant locations. The Laves phase at the bottom resembles punctuation, whereas the Laves phase in the middle is chain-like. In addition, it can be observed that thick and disorderly dislocations frequently accompany of Laves phase.

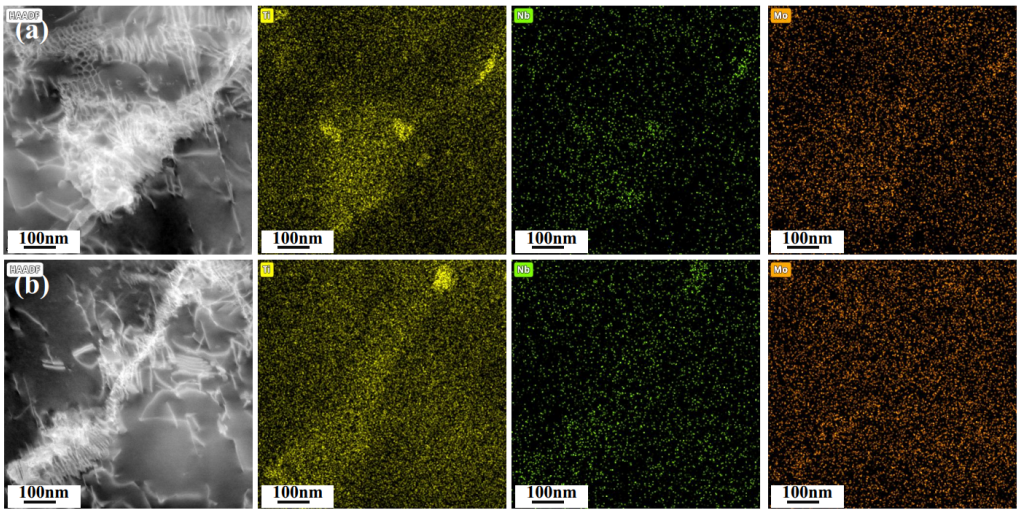


Figure 8. High-angle annular dark field (HAADF)-STEM images and EDS analysis of Laves phase at (**a**) bottom and (**b**) middle.

Figure 9a–c exhibit the SEM images of Laves phase of specimens from bottom to top. The area fraction of Laves phase calculated by Image-Pro Plus software gradually increases from 13.92 to 18.82% then to 19.05%, respectively. Under the impact of STC, as the building's height increase, the area fraction of Laves phase in the lower layers gradually decreases, while that of the upper layers' increases. As a result of inherent heat treatment action of the new layer, a portion of the Laves phase in the lower layers can be remelted during successive scanning [40]. In the meantime, the accumulation of thermal cycles is more conductive to the creation and growth of Laves phase in SLM, and the widening of dendritic spacing coarsens some precipitated phases that fail to remelt. As demonstrated in Figure 9d–f, the morphology of Laves phase evolves from a discrete small point at the bottom to a continuous distributed line at the middle and top, which matches the TEM results.

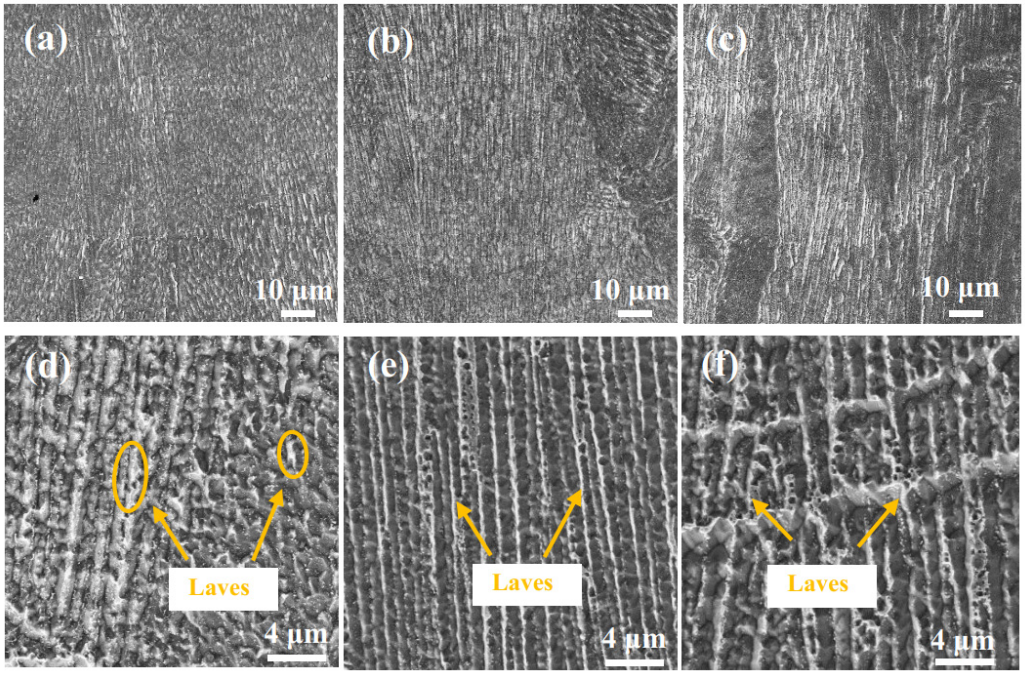


Figure 9. (**a**–**c**) SEM images at bottom to top with low magnification, in which the white regions represent Laves phase to show their approximate area fraction. (**d**–**f**) Magnified images of the three specimens.

It should be emphasized that the brittle nature of Laves phase lowers the alloy's properties [33]. In the presence of Co, the solubility of the Al/Ti element in the matrix is diminished. The substantial segregation of Ti element in Laves phase prevents the synthesis of γ′-Ni3(Al, Ti) despite the absence of Al element segregation. Consequently, despite the high hardness of the Laves phase itself, the reduction in γ′ still results in a drop in the alloy's strength and hardness.

As shown in Figure 10, the microhardness of the FGH96 deposited sample at different building heights was examined to further demonstrate the influence of element segregation under the influence of thermal cycle on the properties. Average microhardness decreased from 347 to 331 HV as deposition height increased. There are three reasons for this phenomenon. Firstly, the increase of Laves phase leads to the decrease of γ′ phase and then lower hardness of the specimens at higher altitudes, as described above. This is also the common view of previous scholars [10]. On the other hand, under the heating effect of the successive thermal cycles, some of the separated refractory elements are partially remelted and diffused into the matrix solute, which has a solid solution-strengthening effect and raises the microhardness of these matrix. Aside from that, generally, the hardness of polycrystalline materials is often correlated with grain boundaries. The relative reduction in grain size will increase the number of grain boundaries and improve the strength and hardness of materials [41], which is also one of the causes of the decrease in microhardness along the building height. The microhardness fluctuation trend of the alloy shows the effect of heat cycling on the precipitation of Laves phase and γ′ phase, solid solution of refractory elements, and grain size.

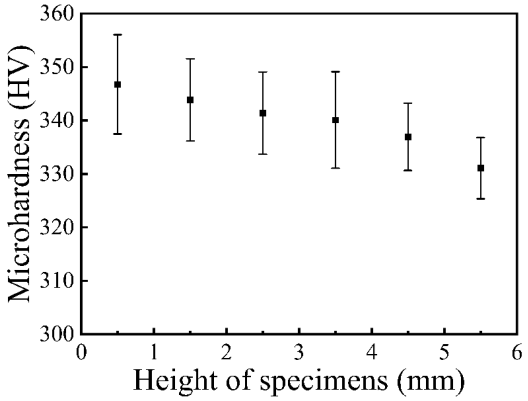


Figure 10. Vickers microhardness of FGH96 by SLM at different heights of specimens.

4. Conclusions

In this study, Ni-based superalloy FGH96 samples were prepared by SLM. The characteristic evolution of texture, dislocation and microsegregation under thermal cycling was analyzed, and the results provide insights into the relationship between microstructure and the mechanical properties of the alloy. The main results are summarized as follows:

The STC coarsens some solidified grains and strengthens the grain growth along the build direction, increasing of texture and HAGBs. Caused by the reduction in STC, a higher cooling rate near the top of the sample increased the degree of undercooling during solidification and refined the grains. As a result, there are 40%, 52% and 30% large-size grains in the bottom, middle and top of the sample, respectively.

There were several dislocations within the grains as a result of their uneven internal tension. Several sets of dislocations perpendicular and at a 45° angle to the grain development direction were discovered in the center of a sample that had undergone stable heat cycles.

Thermal cycling increased the number and size of Laves phase, which inhibited the precipitation of γ' phase. In conjunction with grain coarsening and solid-solution strengthening of pre-deposited layers, these variables worked together to reduce the hardness along the building height.

Supplementary Materials: The following supporting information can be downloaded at: https://www.mdpi.com/article/10.3390/met13010121/s1, Figure S1: Data statistics of specimen bottom measured by EBSD (a) misorientation angle and (b) grain diameter. Figure S2: Data statistics of specimen middle measured by EBSD (a) misorientation angle and (b) grain diameter. Figure S3: Data statistics of specimen top measured by EBSD (a) misorientation angle and (b) grain diameter.

Author Contributions: Conceptualization, formal analysis, writing-original draft, L.L.; methodology, L.L. and S.N.; investigation, Q.W., Y.Z. and H.F.; writing-review and editing, Q.W., R.Z. and F.L.; resources, X.L. All authors have read and agreed to the published version of the manuscript.

Funding: This work was supported by the fund of the state Key Laboratory of Solidification Processing in NWPU (Grant No. SKLSP202112).

Data Availability Statement: Data are available on request from the corresponding author, as they form part of an ongoing study.

Conflicts of Interest: The authors declare no conflict of interest.

References

1. Guan, K.; Wang, Z.M.; Gao, M.; Li, X.Y.; Zheng, X.Y. Effects of processing parameters on tensile properties of selective laser melted 304 stainless steel. *Mater. Des.* **2013**, *50*, 581–586. [CrossRef]
2. Yang, J.J.; Han, J.; Yu, H.C.; Yin, J.; Gao, M.; Wang, Z.M.; Zeng, X.Y. Role of molten pool mode on formability, microstructure and mechanical properties of selective laser melted Ti-6Al-4V alloy. *Mater. Des.* **2016**, *110*, 558–570. [CrossRef]
3. Yin, Y.Y.; Zhang, J.H.; Gao, J.; Zhang, Z.H.; Han, Q.Q.; Zan, Z.L. Laser powder bed fusion of Ni-based Hastelloy X superalloy: Microstructure, anisotropic mechanical properties and strengthening mechanisms. *Mater. Sci. Eng. A* **2021**, *827*, 142076. [CrossRef]

4. Gu, D.D.; He, B.B. Finite element simulation and experimental investigation of residual stresses in selective laser melted Ti-Ni shape memory alloy. *Comput. Mater. Sci.* **2016**, *117*, 221–232. [CrossRef]
5. Yadroitsev, I.; Krakhmalev, P.; Yadroitsava, I. Selective laser melting of Ti6Al4V alloy for biomedical applications: Temperature monitoring and microstructural evolution. *J. Alloys Compd.* **2014**, *583*, 404–409. [CrossRef]
6. Shi, Q.M.; Gu, D.D.; Xia, M.J.; Cao, S.N.; Rong, T. Effects of laser processing parameters on thermal behavior and melting/solidification mechanism during selective laser melting of TiC/Inconel 718 composites. *Opt. Laser Technol.* **2016**, *84*, 9–22. [CrossRef]
7. Masoomi, M.; Thompson, S.M.; Shamsaei, N. Laser powder bed fusion of Ti-6Al-4V parts: Thermal modeling and mechanical implications. *Int. J. Mach. Tools Manuf.* **2017**, *118*, 73–90. [CrossRef]
8. Gu, D.D.; Shi, Q.M.; Lin, K.J.; Xi, L.X. Microstructure and performance evolution and underlying thermal mechanisms of Ni-based parts fabricated by selective laser melting. *Addit. Manuf.* **2018**, *22*, 265–278. [CrossRef]
9. Huang, W.B.; Zhang, Y.M. Finite element simulation of thermal behavior in single-track multiple-layers thin wall without-support during selective laser melting. *J. Manuf. Process.* **2019**, *42*, 139–148. [CrossRef]
10. Yang, H.H.; Yang, J.J.; Huang, W.P.; Wang, Z.M.; Zeng, X.Y. The printability, microstructure, crystallographic features and microhardness of selective laser melted Inconel 718 thin wall. *Mater. Des.* **2018**, *156*, 407–418. [CrossRef]
11. Mahmoudi, M.; Elwany, A.; Yadollahi, A.; Thompson, S.M.; Bian, L.K.; Shamsaei, N. Mechanical properties and microstructural characterization of selective laser melted 17–4 PH stainless steel. *Rapid. Prototyp. J.* **2017**, *23*, 280–294. [CrossRef]
12. Mohr, G.; Scheuschner, N.; Hilgenberg, K. In situ heat accumulation by geometrical features obstructing heat flux and by reduced inter layer times in laser powder bed fusion of AISI 316L stainless steel. *Procedia CIRP* **2020**, *94*, 155–160. [CrossRef]
13. Wang, X.Q.; Chou, K. Effects of thermal cycles on the microstructure evolution of Inconel 718 during selective laser melting process. *Addit. Manuf.* **2017**, *18*, 1–14. [CrossRef]
14. Wang, X.; Keya, T.; Chou, K. Build height effect on the Inconel 718 parts fabricated by selective laser melting. *Procedia Manuf.* **2016**, *5*, 1006–1017. [CrossRef]
15. Wang, X.Q.; Gong, X.B.; Chou, K. Review on powder-bed laser additive manufacturing of Inconel 718 parts. *Proc. Inst. Mech. Eng. Part B J. Eng. Manuf.* **2017**, *231*, 1890–1903. [CrossRef]
16. Sanchez, S.; Smith, P.; Xu, Z.K.; Gaspard, G.; Hyde, C.J.; Wits, W.W.; Ashcroft, I.A.; Chen, H.; Clare, A.T. Powder Bed Fusion of nickel-based superalloys: A review. *Int. J. Mach. Tools Manuf.* **2021**, *165*, 103729. [CrossRef]
17. Cam, G.; Kocak, M. Progress in joining of advanced materials. *Int. Mater. Rev.* **1998**, *43*, 1–44. [CrossRef]
18. Montazeri, M.; Ghaini, F.M. The liquation cracking behavior of IN738LC superalloy during low power Nd:YAG pulsed laser welding. *Mater. Charact.* **2021**, *67*, 65–73. [CrossRef]
19. Ojo, O.A.; Richards, N.L.; Chaturvedi, M.C. Contribution of constitutional liquation of gamma prime precipitate to weld HAZ cracking of cast Inconel 738 superalloy. *Scr. Mater.* **2004**, *50*, 641–646. [CrossRef]
20. Tian, X.; Zhang, Y.W.; Yue, C. Effect of Hf and Zr Contents on Stress-rupture and Fatigue Crack Growth Rate Performances in FGH96 PM Superalloy. *J. Iron Steel Res. Int.* **2014**, *21*, 382–388.
21. Hua, D.Y.; Wang, T.; Ma, Q.H.; Liu, X.; Shang, L.H.; Li, D.; Pan, J.C.; Wang, R.Q. Effect of inclusions on low cycle fatigue lifetime in a powder metallurgy nickel-based superalloy FGH96. *Int. J. Fatigue* **2018**, *118*, 237–248. [CrossRef]
22. Peng, Z.C.; Zou, J.W.; Wang, X.Q. Microstructural characterization of dislocation movement during creep in powder metallurgy FGH96 superalloy. *Mater. Today Commun.* **2020**, *25*, 101361. [CrossRef]
23. Hao, Z.B.; Tian, T.; Li, X.G.; Huang, Y.H.; Peng, S.Q.; Zhu, Q.; Ge, C.C. Effects of hot processes on microstructure evolution and tensile properties of FGH4096 Ni-based superalloy processed by Laser Powder Bed Fusion. *Mater. Sci. Eng. A* **2021**, *804*, 140775. [CrossRef]
24. Hao, Z.B.; Tian, T.; Peng, S.Q.; Ge, C.C.; Li, X.G.; Jia, C.L.; Guo, C.; Zhu, Q. Effect of Heat Treatment on Microstructure and Properties of FGH4096M Superalloy Processed by Selective Laser Melting. *Met. Mater. Int.* **2020**, *26*, 1270–1285. [CrossRef]
25. Li, F.L.; Bai, Y.R.; Meng, L.C.; Fu, R.; Zhong, Y.; Du, J.H.; Yin, F.J.; Feng, D. Impact of aging heat treatment on microstructure and mechanical properties of a newly developed GH4096 disk superalloy. *Mater. Charact.* **2020**, *161*, 110175. [CrossRef]
26. Xu, J.Y.; Ding, Y.T.; Gao, Y.B.; Wang, H.; Hu, Y.; Zhang, D. Grain refinement and crack inhibition of hard-to-weld Inconel 738 alloy by altering the scanning strategy during selective laser melting. *Mater. Des.* **2021**, *209*, 109940. [CrossRef]
27. Popovich, V.A.; Borisov, E.V.; Popovich, A.A.; Sufiiarov, V.S.; Masaylo, D.V.; Alzina, L. Functionally graded Inconel 718 processed by additive manufacturing: Crystallographic texture, anisotropy of microstructure and mechanical properties. *Mater. Des.* **2017**, *114*, 441–449. [CrossRef]
28. Huang, M.; Zhuo, L.C.; Xiong, J.C.; Li, J.R.; Zhu, J. Core structure of a <100> superdislocations in a single-crystal superalloy during high-temperature and low-stress creep. *Philos. Mag. Lett.* **2015**, *95*, 496–503. [CrossRef]
29. Wei, H.L.; Mazumder, J.; DebRoy, T. Evolution of solidification texture during additive manufacturing. *Sci. Rep.* **2015**, *5*, 16446. [CrossRef]
30. Sun, S.H.; Hagihara, K.; Nakano, T. Effect of scanning strategy on texture formation in Ni-25 at.% Mo alloys fabricated by selective laser melting. *Mater. Des.* **2018**, *140*, 307–316. [CrossRef]
31. Basu, B.; Date, A.W. Rapid solidification following laser melting of pure metals - II. Study of pool and solidification characteristics. *Int. J. Heat Mass Tran.* **1992**, *35*, 1059–1067. [CrossRef]

32. Loretto, M.H.; Godfrey, A.B.; Hu, D.; Blenkinsop, P.A.; Jones, I.P.; Cheng, T.T. The influence of composition and processing on the structure and properties of TiAl-based alloys. *Intermetallics* **1998**, *6*, 663–666. [CrossRef]
33. Wang, H.M.; Zhang, J.H.; Tang, Y.J.; Hu, Z.Q.; Yukawa, N.; Morinaga, M.; Murata, Y. Rapidly solidified MC carbide morphologies of a laser-glazed single-crystal nickel-base superalloy. *Mater. Sci. Eng. A* **1992**, *156*, 109–116. [CrossRef]
34. Denlinger, E.R.; Gouge, M.; Irwin, J.; Michaleris, P. Thermomechanical model development and in situ experimental validation of the Laser Powder-Bed Fusion process. *Addit. Manuf.* **2017**, *16*, 73–80. [CrossRef]
35. Li, Y.L.; Zhou, K.; Tan, P.F.; Tor, S.B.; Chua, C.K.; Leong, K.F. Modeling temperature and residual stress fields in selective laser melting. *Int. J. Mech. Sci.* **2018**, *136*, 24–35. [CrossRef]
36. Liu, L.; Ding, Q.Q.; Zhong, Y.; Zhou, J.; Wu, J.; Chiu, Y.L.; Li, J.; Zhang, Z.; Yu, Q.; Shen, Z. Dislocation network in additive manufactured steel breaks strength-ductility trade-off. *Mater. Today* **2017**, *21*, 354–361. [CrossRef]
37. Bertsch, K.M.; de Bellefon, G.M.; Kuehl, B.; Thoma, D.J. Origin of dislocation structures in an additively manufactured austenitic stainless steel 316L. *Acta Mater.* **2020**, *199*, 19–33. [CrossRef]
38. Nie, P.L.; Ojo, O.A.; Li, Z.G. Numerical Modeling of Microstructure Evolution during Laser Additive Manufacturing of a Nickel-based Superalloy. *Acta Mater.* **2014**, *77*, 85–95. [CrossRef]
39. Xiao, H.; Li, S.M.; Xiao, W.J.; Li, Y.Q.; Cha, L.M.; Mazumder, J.; Song, L.J. Effects of laser modes on Nb segregation and Laves phase formation during laser additive manufacturing of nickel-based superalloy. *Mater. Lett.* **2017**, *188*, 260–262. [CrossRef]
40. Parimi, L.L.; Ravi, G.A.; Clark, D.; Attallah, M.M. Microstructural and texture development in direct laser fabricated IN718. *Mater. Charact.* **2014**, *89*, 102–111. [CrossRef]
41. Yu, H.H.; Xin, Y.C.; Wang, M.Y.; Liu, Q. Hall-Petch relationship in Mg alloys: A review. *J. Mater. Sci. Technol.* **2018**, *34*, 248–256. [CrossRef]

Disclaimer/Publisher's Note: The statements, opinions and data contained in all publications are solely those of the individual author(s) and contributor(s) and not of MDPI and/or the editor(s). MDPI and/or the editor(s) disclaim responsibility for any injury to people or property resulting from any ideas, methods, instructions or products referred to in the content.